Link between the photonic and electronic topological phases in artificial graphene

Sylvain Lannebère[1] and Mário G. Silveirinha[1,2,*]

[1]*Department of Electrical Engineering, University of Coimbra and Instituto de Telecomunicações, 3030-290 Coimbra, Portugal*
[2]*University of Lisbon–Instituto Superior Técnico, Department of Electrical Engineering, 1049-001 Lisboa, Portugal*

In recent years the study of topological phases of matter has emerged as a very exciting field of research, both in photonics and in electronics. However, up to now the electronic and photonic properties have been regarded as totally independent. Here we establish a link between the *electronic* and the *photonic* topological phases of the same material system and theoretically demonstrate that they are intimately related. We propose a realization of the Haldane model as a patterned two-dimensional electron gas and determine its optical response using the Kubo formula. It is shown that the electronic and photonic phase diagrams of the patterned electron gas are strictly related. In particular, the system has a trivial photonic topology when the inversion symmetry is the prevalent broken symmetry, whereas it has a nontrivial photonic topology for a dominant broken time-reversal symmetry, similar to the electronic case. To confirm these predictions, we numerically demonstrate the emergence of topologically protected unidirectional electromagnetic edge states at the interface with a trivial photonic material.

I. INTRODUCTION

The discovery of topological phases of matter was a major breakthrough in modern condensed-matter and electromagnetics research [1–5]. The material topology is determined by the global properties of the electronic or photonic bands, which are characterized by some topological invariant, e.g., the Chern number. The topological properties are robust against smooth variations of the system parameters and can only be changed through a phase transition that involves the exchange of topological numbers of different bands by closing and reopening of a band gap. This characteristic makes the topological properties quite insensitive to fabrication imperfections. Furthermore, perhaps the most remarkable feature of topological materials is their ability to support unidirectional edge states or spin-polarized edge states at the interface with ordinary insulators [6–10]. This property was demonstrated theoretically and experimentally in a plethora of systems relying on nonreciprocal [11–27] and reciprocal materials [28–35]. In particular, topological systems are quite unique platforms for the development of integrated one-way, defect-immune electronic and photonic guiding devices, even though other solutions not based on topological properties may exist [35].

Topological materials can be divided into two categories depending on whether or not they remain invariant under the time-reversal operation. Historically, the importance of the time-reversal symmetry in the topology of physical systems was underscored by Haldane who demonstrated in his seminal work [36] that a broken time-reversal symmetry is the key ingredient to obtain a quantized electronic Hall phase. This important result was some decades later extended to electromagnetism [9], and since then a variety of strategies to obtain nontrivial photonic topological phases with a broken time-reversal symmetry was proposed [13,15–19,22,24,25,27].

In parallel, recent studies about the reflection of a light beam on 2D materials with a quantized Hall conductivity [37,38] have revealed interesting connections between nontrivial electronic and photonic topological properties (namely quantized Imbert-Fedorov, Goos-Hänchen, and photonic spin Hall shifts).

Inspired by these ideas, here we show using the Haldane model [36] how a topologically nontrivial electronic material with a quantized Hall conductivity in the static limit can be used as a building block to create a topologically nontrivial photonic material. It is proven that analogous to the electronic counterpart, the photonic band structure is topologically nontrivial when the time-reversal symmetry is the dominant broken symmetry. Thus, our work establishes a direct link between the electronic and photonic topological properties.

The paper is organized as follows. In Sec. II A we propose a patterned two-dimensional (2D) electron gas (2DEG) with the symmetries of the Haldane model. The structure consists of an array of scattering centers organized in a honeycomb lattice (often referred to as "artificial graphene" [39,40]) under the influence of a fluctuating static magnetic field with zero mean value. Using a "first-principles" calculation method, we find the values of the Haldane tight-binding parameters and derive the electronic topological phase diagram. In Sec. III the dynamic conductivity response of the 2D material is calculated with the Kubo formula. The conductivity is used in Sec. III to characterize the photonic properties of the system and derive the natural modes. The photonic Chern numbers are found with an extension of the theory of [41]. It is shown that the transition from a trivial to a nontrivial electronic topological phase in Haldane graphene induces a photonic topological phase transition. Thereby, we unveil the intimate relation

---

*To whom correspondence should be addressed: mario.silveirinha@co.it.pt

between the electronic and photonic topological properties. Furthermore, it is demonstrated with full-wave simulations that the nontrivial photonic topological phase enables the propagation of unidirectional edge states at the interface with an ordinary light "insulator" (i.e., an opaque material with no light states). A brief overview of the main findings of the article is presented in Sec. V.

II. HALDANE ARTIFICIAL GRAPHENE

A. Overview of the Haldane model

The Haldane model is a generalization of the tight-binding Hamiltonian of graphene to systems with a broken inversion symmetry (IS) and/or a broken time-reversal symmetry (TRS) [36]. Analogous to the graphene case, the Haldane Hamiltonian describes a 2D hexagonal lattice with two scattering centers per unit cell. However, in the Haldane model the two sublattices are allowed to be different, and in the model this feature is described by a mass term M, which may be positive or negative. When the two sublattices are identical the mass term vanishes and the 2D material is invariant under the inversion operation. Furthermore, the Haldane model takes into account the possible effect of a nontrivial space-varying static magnetic field with a net flux equal to zero. The magnetic field is responsible for breaking the TRS.

The Taylor expansion of the Haldane's Hamiltonian near K and K' is given by

$$H(\mathbf{K} + \mathbf{q}) = -3t_2 \cos(\phi) \cdot \mathbf{1} + \alpha_K \cdot \boldsymbol{\sigma}_z$$
$$- \tfrac{3}{2}t_1 a(q_x \boldsymbol{\sigma}_x + q_y \boldsymbol{\sigma}_y), \quad (1a)$$

$$H(\mathbf{K'} + \mathbf{q}) = -3t_2 \cos(\phi) \cdot \mathbf{1} + \alpha_{K'} \cdot \boldsymbol{\sigma}_z$$
$$- \tfrac{3}{2}t_1 a(q_x \boldsymbol{\sigma}_x - q_y \boldsymbol{\sigma}_y), \quad (1b)$$

where a is the nearest-neighbors distance, $\mathbf{q} = q_x \hat{\mathbf{x}} + q_y \hat{\mathbf{y}}$ is the wave vector taken relatively to K or K', t_1 and t_2 are the nearest neighbors (in different sublattices) and next-nearest neighbors (in the same sublattice) hopping energies, respectively, $\boldsymbol{\sigma}_i$'s are the Pauli matrices, and

$$\alpha_K = M - 3\sqrt{3}t_2 \sin(\phi), \quad (2a)$$

$$\alpha_{K'} = M + 3\sqrt{3}t_2 \sin(\phi) \quad (2b)$$

are the terms resulting from breaking the IS and/or the TRS at K and K', respectively. These parameters vanish in pristine graphene. The phase factor ϕ is determined by the integral of the magnetic vector potential along a path that joins next-nearest neighbors [36].

The Haldane Hamiltonian leads to a two-band model whose upper and lower band eigenfunctions, denoted by $|+\rangle$ and $|-\rangle$, respectively, have energies $E_\pm$ given by

$$E_\pm(K) = -3t_2 \cos(\phi) \pm \tfrac{1}{2}\sqrt{(3t_1 aq)^2 + 4\alpha_K^2}, \quad (3a)$$

$$E_\pm(K') = -3t_2 \cos(\phi) \pm \tfrac{1}{2}\sqrt{(3t_1 aq)^2 + 4\alpha_{K'}^2}. \quad (3b)$$

Of course, when the inversion and time-reversal symmetries are preserved $\alpha_K = \alpha_{K'} = 0$, and one recovers the band diagram of pristine graphene with Dirac cones at K and K'. On the other hand, a nonzero α_K ($\alpha_{K'}$) opens an energy gap

$E_{g,K} = 2|\alpha_K|$ ($E_{g,K'} = 2|\alpha_{K'}|$) at K (K') between the $|+\rangle$ and $|-\rangle$ bands. Remarkably the electronic phases obtained by breaking predominantly the TRS [sgn(α_K) $\neq$ sgn($\alpha_{K'}$)] or the IS [sgn(α_K) = sgn($\alpha_{K'}$)] are topologically distinct, leading to different electronic Chern numbers ν [36]. The Chern number of the valence band $|-\rangle$ can be written as (see Appendix A)

$$\nu = \tfrac{1}{2}[\text{sgn}(\alpha_K) - \text{sgn}(\alpha_{K'})]. \quad (4)$$

For convenience, we will refer in the following to the electronic phase with sgn(α_K) $\neq$ sgn($\alpha_{K'}$) (which has a Chern number $\nu = \pm 1$ and thereby a nonzero Hall conductivity) as the "Hall phase" and to the electronic phase with sgn(α_K) = sgn($\alpha_{K'}$) (which has vanishing Chern number $\nu = 0$ and vanishing static Hall conductivity) as the "insulating phase."

B. Haldane model in a 2DEG

Next, we outline how the Haldane model may be implemented by modifying the "artificial graphene" structure proposed in [39]. The main objective is to give some visualization of the system under study and at the same time obtain an estimate for the Haldane's tight-binding Hamiltonian parameters.

Artificial graphene consists of a 2DEG under the influence of a periodic electrostatic potential $V(\mathbf{r})$ with the honeycomb symmetry. As demonstrated in [39,40] such a system is fully equivalent to graphene in the sense that near the Dirac points the electrons are described by a massless Dirac Hamiltonian with a linear energy dispersion. Therefore, by breaking the TRS and/or the IS it should be possible to emulate the Haldane model in this platform.

Following Haldane's idea, a broken IS is implemented by considering different scattering centers for each of the sublattices of the artificial graphene. In our model, the scattering centers are characterized by constant potentials V_1 and V_2, and are depicted in Fig. 1(a) as circles with different colors. The region outside the circles has $V = 0$. The broken TRS is achieved with a zero mean-value static magnetic field $\mathbf{B}$. The corresponding magnetic potential $\mathbf{A}$, defined such that $\mathbf{B} = \nabla \times \mathbf{A}$, is supposed to yield a nontrivial flux $\int \mathbf{A} \cdot \mathbf{dl}$ when the starting and ending points of the integration path are next-nearest neighbors, and a trivial flux when the starting and ending points are nearest neighbors. As illustrated in Fig. 1(a), a magnetic vector potential $\mathbf{A}$ of the form

$$\mathbf{A}(\mathbf{r}) = \frac{3B_0 a^2}{16\pi^2}\{\mathbf{b}_1 \sin(\mathbf{b}_1 \cdot \mathbf{R}) + \mathbf{b}_2 \sin(\mathbf{b}_2 \cdot \mathbf{R}) +$$
$$(\mathbf{b}_1 + \mathbf{b}_2)\sin([\mathbf{b}_1 + \mathbf{b}_2] \cdot \mathbf{R})\} \times \hat{\mathbf{z}} \quad (5)$$

fulfills such requirements. Here B_0 is the peak magnetic field amplitude in Tesla, $\mathbf{R} = \mathbf{r} - \mathbf{r}_c$ where $\mathbf{r}_c$ determines the coordinates of the honeycomb cell's center [Fig. 1(a)], and the $\mathbf{b}_i$'s with $i = 1, 2$ are the reciprocal lattice primitive vectors. Both $\mathbf{A}$ and $\mathbf{B}$ are represented in the honeycomb lattice in Fig. 1(a). Note that the magnetic field is directed along the z direction, perpendicular to the 2D electron gas. Similar to Ref. [40], it is supposed that the nearest-neighbors distance is $a = 150$ nm and that the radius R_0 of the scattering centers satisfies $R_0/a = 0.35$. Even though challenging, in principle the required magnetic field distribution can be created at the nanoscale by nanostructuring permanent magnets.
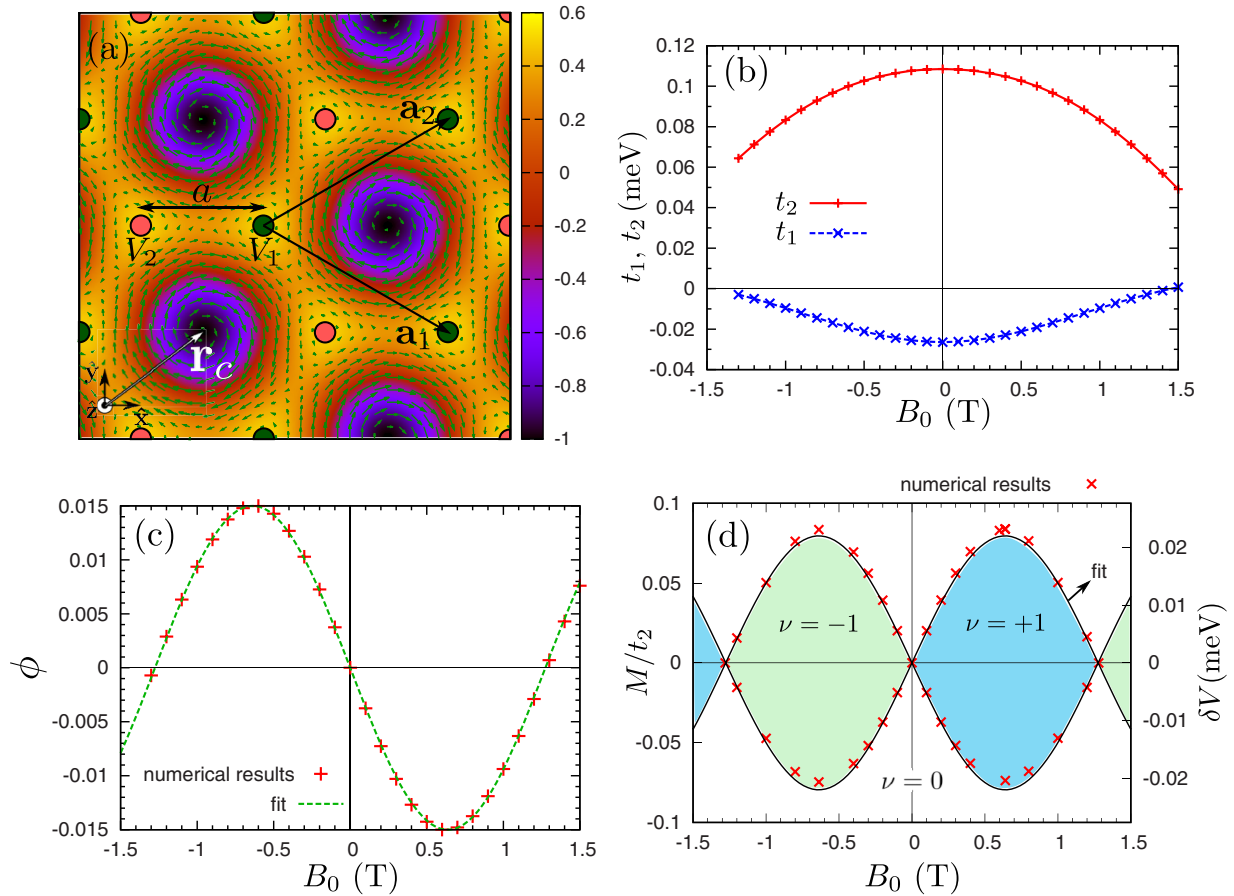
FIG. 1. (a) Density plot of the magnetic field **B** (color scale) and of the magnetic vector potential **A** (arrows) used to break the TRS. The scattering centers (green and pink circles, associated with the electrostatic potentials V_1 and V_2, respectively), as well as the lattice primitive vectors are represented on the top of the fields. (b) Variation of the tight-binding energies t_1 and t_2 (in meV) obtained from first-principles calculations as a function of the magnetic field's magnitude B_0 for $V_1 = V_2 = -0.8$ meV. (c) Variation of the parameter ϕ obtained from a first-principles calculations as a function of B_0 for $V_1 = V_2 = -0.8$ meV. (d) Phase diagram giving the electronic Chern number ν as a function of B_0 and M/t_2 (or equivalently δV) for the lower energy band. The boundaries between the different topological phases were obtained by interpolation of the first-principles numerical results (red crosses).

The tight-binding parameters depend on V_1, V_2, and B_0. They are numerically found from first-principles calculations using the effective medium formalism for electron waves developed in [42] and extended to artificial graphene in [40] (we use the expression first principles in a broad sense with the meaning that the tight-binding parameters are found from a microscopic model). The first step of the method is to solve the Schrödinger equation governing the electron wave propagation in the 2DEG, starting from the "microscopic" Hamiltonian

$$\hat{H}_{\mathrm{mic}} = \frac{1}{2m_b}[\hat{\mathbf{p}} + e\mathbf{A}(\mathbf{r})]^2 + V(\mathbf{r}), \qquad (6)$$

where $-e$ is the electron charge, $V(\mathbf{r}) = V_1(\mathbf{r}) + V_2(\mathbf{r})$ is the periodic electrostatic potential, **A** is given by (5), and the electron effective mass m_b is as in Ref. [39]: $m_b = 0.067m$, with m the electron rest mass. In the spirit of Haldane's work, the spin interaction is neglected. The Schrödinger equation is numerically solved with the finite differences method [40]. Next, following the homogenization process detailed in [40], we obtain a 2×2 effective Hamiltonian that determines the stationary states and the energy dispersion. A detailed analysis (not shown) of the energy diagrams obtained for different values of V_1, V_2, and B_0 shows that the Haldane model correctly describes the physics of the 2DEG near the Dirac points. Furthermore, the tight-binding parameters can be calculated from a Taylor expansion of the effective Hamiltonian near the Dirac points [40], which is found to be of the forms (1a) and (1b).

The numerically calculated tight-binding parameters are represented in Figs. 1(b) and 1(c) as a function of the magnetic field intensity for $V_1 = V_2 = -0.8$ meV. Note that when $V_1 = V_2$ the mass parameter vanishes ($M = 0$). Curiously, unlike in graphene, in our system $|t_2| > |t_1|$. The hopping constant t_1 has a value comparable with that found in [40]. More interestingly, it can be seen that the parameter ϕ obtained from the first-principles simulations is a periodic function of B_0 and hence is bounded. This feature is not present in the Haldane model wherein ϕ is regarded as an arbitrary real-valued number proportional to B_0. The peak value of ϕ found here implies that the maximum energy gap $6\sqrt{3}t_2\sin(\phi)$, due to the applied magnetic field, is on the order of $0.156 \cdot t_2$. The peak ϕ is reached for $B_0 \approx 0.64$ T, which may be difficult to create considering that the magnetic field varies at the nanoscale.

To characterize the topology of the 2DEG, we numerically found the combination of parameters B_0 and δV for which the band gap closes at one of the Dirac points, taking $V_1 = -0.8$ meV and $V_2 = V_1 + \delta V$. A nontrivial δV implies a nonzero tight-binding mass parameter M. The calculated phase diagram is represented in Fig. 1(d) and shows the combination of parameters M and B_0 for which the band gap closes. Consistent with [36], we find that when a band gap closes and reopens there is a topological phase transition and the electronic Chern number changes by one unity. The Chern numbers associated with the energy band $|-\rangle$ are indicated in Fig. 1(d). The electronic Chern number determines the static Hall conductivity in the limit of a zero temperature when the Fermi level is in the band gap [43,44]. The calculated phase diagram agrees perfectly with Haldane's theory [36], since the periodicity of ϕ with B_0 induces also a periodicity in the phase diagram. Thus, similar to [36], the broken IS phase corresponds to a trivial electronic Chern number $\nu = 0$, whereas the broken TRS phase corresponds to a phase with $\nu \neq 0$.

As a partial summary, we outlined a physical realization of the abstract notions developed in [36], relying on "artificial graphene" and on the periodic magnetic field potential distribution (5). Our study gives the tight-binding parameters obtained from first-principles calculations. In the simulations it was assumed that $a = 150$ nm but the design parameters can be renormalized to other values of a through a simple dimensional analysis (e.g., a reduction of a by a factor of 2 implies an increase of all the involved energies and of B_0 by a factor of 4). Even though the practical implementation of the Haldane model in a 2DEG is admittedly very challenging, our study provides a simple visualization of the concepts introduced in [36]. In the rest of the article we use the tight-binding parameters obtained in this section and it is assumed that the relation between B_0 and ϕ corresponds to the fit of Fig. 1(c): $\phi = -0.015 \sin\left(\frac{2\pi B_0}{2.56}\right)$, with B_0 in Tesla.

III. DYNAMIC CONDUCTIVITY OF HALDANE GRAPHENE

In order to characterize the photonic properties of "Haldane graphene," next we derive its dynamic conductivity with Kubo's linear response theory [45]. It is assumed that the valence band $|-\rangle$ is completely filled (the chemical potential μ is in the gap) and that the temperature satisfies $k_B T \ll E_g$, with k_B the Boltzmann constant and $E_g = 2\min(|\alpha_K|, |\alpha_{K'}|)$ the gap energy. In these conditions, the Hall conductivity in the static limit is determined by the electronic Chern number. Furthermore, the intraband conductivity term vanishes and thereby the dynamic conductivity is given by [46–48]

$$\boldsymbol{\sigma}^{\mathrm{gr}}(\omega) = \frac{ie^2\hbar}{(2\pi)^2} \sum_{m \neq n} \int \int \frac{f(E_{m\mathbf{k}}) - f(E_{n\mathbf{k}})}{(E_{m\mathbf{k}} - E_{n\mathbf{k}} - \hbar\omega)(E_{m\mathbf{k}} - E_{n\mathbf{k}})}$$
$$\times \langle n\mathbf{k}|\hat{\mathbf{v}}|m\mathbf{k}\rangle \langle m\mathbf{k}|\hat{\mathbf{v}}|n\mathbf{k}\rangle \, d^2\mathbf{k}, \quad (7)$$

where f is the Fermi distribution function, $\hat{\mathbf{v}} = \frac{1}{\hbar}\frac{\partial \hat{H}}{\partial \mathbf{k}}$ is the velocity operator, and the sum is over the different bands $|+\rangle$ and $|-\rangle$. It is implicit that the contributions of both Dirac points are included. Somewhat lengthy but otherwise straightforward calculations based on the continuum version of the Haldane

model show that when thermal effects are negligible ($k_B T \ll E_g$) the dynamic conductivity is of the form

$$\boldsymbol{\sigma}^{\mathrm{gr}}(\omega) = \sigma_t \mathbf{1}_t - \sigma_H \hat{\mathbf{z}} \times \mathbf{1}_t, \quad (8a)$$

where $\mathbf{1}_t = \hat{\mathbf{x}}\hat{\mathbf{x}} + \hat{\mathbf{y}}\hat{\mathbf{y}}$. Thus, in general the material response is gyrotropic, with the antidiagonal elements of the conductivity tensor given by $\sigma_{xy} = -\sigma_{yx} = \sigma_H$ and the diagonal elements determined by $\sigma_{xx} = \sigma_{yy} = \sigma_t$. For ω real valued with $\hbar|\omega| < E_g$ the conductivity elements are given by

$$\sigma_t = -i\sigma_0 \frac{\mathrm{sgn}(\omega)}{4}\left(G(\Omega_K) + G(\Omega_{K'}) + \frac{G(\Omega_K) - |\Omega_K|}{\Omega_K^2}\right.$$
$$\left. + \frac{G(\Omega_{K'}) - |\Omega_{K'}|}{\Omega_{K'}^2}\right), \quad (8b)$$

$$\sigma_H = \frac{\sigma_0}{2}\left(\frac{G(\Omega_{K'})}{\Omega_{K'}} - \frac{G(\Omega_K)}{\Omega_K}\right). \quad (8c)$$

In the above, $\Omega_i = \hbar|\omega|/(2\alpha_i)$ is a normalized frequency ($i = K, K'$), $G(\Omega_i) = \tanh^{-1}(|\Omega_i|)$, and $\sigma_0 = \frac{e^2}{\hbar}$. Remarkably, when $k_B T/E_g \to 0$ the conductivity is independent of the nearest neighbor hopping energy t_1. In the spirit of the Haldane model, it was supposed in the conductivity calculation that the Hamiltonian describes some particular (nondegenerate) electron spin. We note that the conductivity (8a) is calculated for a system with no boundaries. In practice, the material sample has a finite size and this may lead to corrections to the bulk conductivity. These corrections will depend on an additional length scale related to the size of the sample. Considering such corrections would require a more sophisticated analysis which is out of the intended scope of our study.

A direct inspection of Eq. (8c) reveals that in the absence of a magnetic field ($\phi = 0$), i.e., when the parameters Ω_K and $\Omega_{K'}$ are equal, the Hall conductivity is precisely zero. In contrast, for a nonzero magnetic field two distinct situations can occur depending on which broken symmetry is prevalent. Indeed, for relatively low frequencies ($\hbar\omega \ll E_g$) the function G may be approximated by $G(\Omega_i) \approx |\Omega_i| + \frac{|\Omega_i|^3}{3}$. In these conditions, the conductivities (8b) and (8c) reduce to

$$\sigma_t \approx -i\sigma_0 \frac{\omega}{\omega_0}, \quad (9a)$$

$$\sigma_H \approx \frac{\sigma_0}{2}[\mathrm{sgn}(\alpha_{K'}) - \mathrm{sgn}(\alpha_K)] = -\sigma_0 \nu, \quad (9b)$$

with $\omega_0^{-1} = \frac{\hbar}{6}\left(\frac{1}{|\alpha_K|} + \frac{1}{|\alpha_{K'}|}\right)$. Equation (9b) confirms that the Hall conductivity in the static limit is quantized and is determined by the electronic Chern number ν given by (4), which is the TKNN result [43,44]. Thus, consistent with Haldane's work, we find that the insulating phase has a trivial conductivity in the static limit, whereas the Hall phase has a quantized Hall conductivity. Furthermore, near $\omega = 0$ the diagonal term σ_t is a linear function of the frequency with slope ω_0^{-1}.

The evolution of the Haldane graphene conductivity as a function of frequency for the insulating and Hall phases is represented in Fig. 2. In agreement with the phase diagram of Fig. 1(d) and with Eq. (9b), it is seen that the Hall conductivity at $\omega = 0$ is determined by the Chern number and is nontrivial only in the Hall phase. Perhaps the most striking feature that discriminates the two different phases is the magnitude ratio
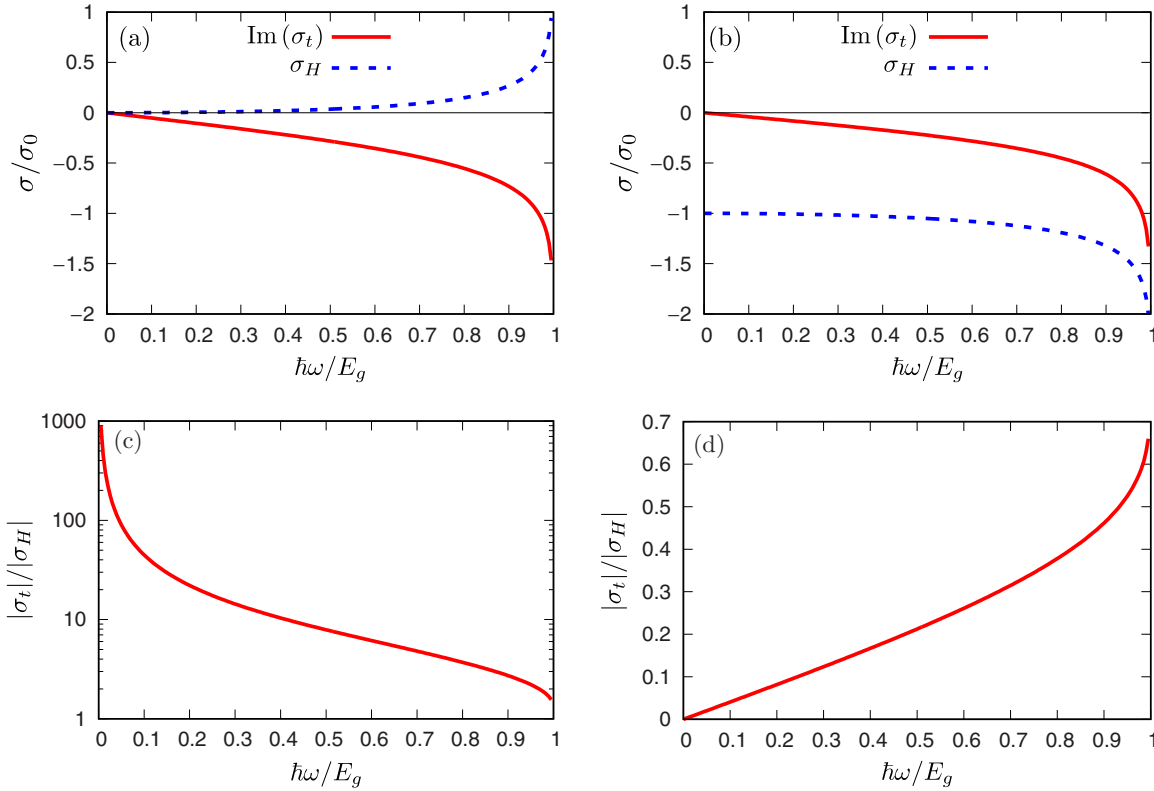
FIG. 2. (a) and (b) Plot of the normalized conductivity of Haldane graphene for frequencies ω smaller than the gap frequency $E_g/\hbar$ in (a) the insulating phase $B_0 = 0.075$ T corresponding to $\alpha_K/\hbar \approx 9.76$ GHz and $\alpha_{K'}/\hbar \approx 5.43$ GHz and (b) the Hall phase $B_0 = 0.64$ T corresponding to $\alpha_K/\hbar \approx 19.5$ GHz and $\alpha_{K'}/\hbar \approx -4.24$ GHz. (c) and (d) Ratio $|\sigma_t|/|\sigma_H|$ for the conductivities depicted in (a) and (b), respectively. In the plots $M = 5 \times 10^{-3}$ meV, $t_1 = -0.02$ meV, and $t_2 = 0.1$ meV.

$|\sigma_t|/|\sigma_H|$, represented in Figs. 2(c) and 2(d). Remarkably, it is much greater than unity for the insulating phase and near zero for the Hall phase. The singularities in the conductivity components near electronic band gap frequency are of logarithmic type.

Figure 3 represents the parameter ω_0^{-1} and the static Hall conductivity σ_H as a function of the peak magnetic field B_0 for a mass parameter $M/t_2 = 0.05$. By comparison with the phase diagram of Fig. 1(d), it is seen that the Hall conductivity σ_H experiences discontinuous jumps at the topological phase transitions, whereas the component σ_t remains continuous in the quasistatic limit. It is worth pointing out that the

tight-binding parameters used in Fig. 2 (which will be adopted in the rest of the article) yield values for ω_0^{-1} that are comparable for both phases.

To conclude, it is highlighted that Haldane graphene in the Hall phase has a quasistatic conductivity response analogous to that of a magnetized plasma. Indeed, in the limit $\omega \to 0$ a lossless magnetized plasma is also characterized by a purely imaginary σ_t that vanishes in the static limit and by a nonzero (but not quantized) σ_H [49]. However, the two systems are generically rather different. While a decrease of the magnetic field amplitude B_0 transforms Haldane graphene into an insulating material ($\sigma_{\omega=0} = 0$), the conductivity of
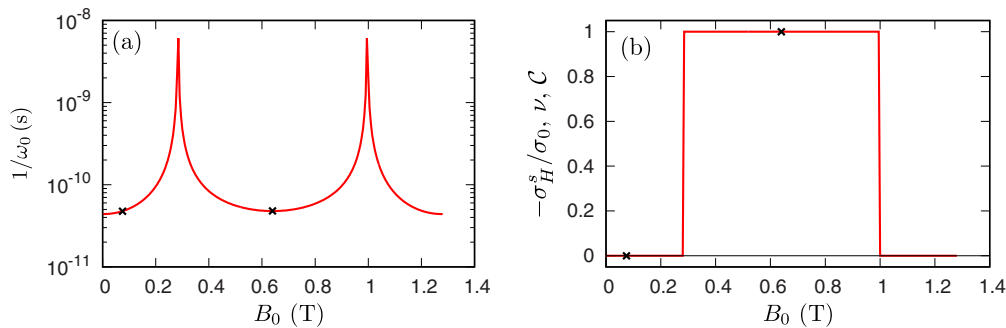

FIG. 3. (a) Slope ω_0^{-1} of σ_t in the quasistatic limit as a function of the magnetic field B_0. (b) Normalized static Hall conductivity $-\sigma_H^s$ and electronic Chern number ν as a function of the magnetic field B_0. The plot also depicts the (positive frequency branch) photonic Chern number $\mathcal{C}$ for the structure of Fig. 4. In both panels $t_1 = -0.02$ meV, $t_2 = 0.1$ meV, $M = 5 \times 10^{-3}$ meV. The two black crosses mark the values of B_0 used in the plots of Fig. 2.
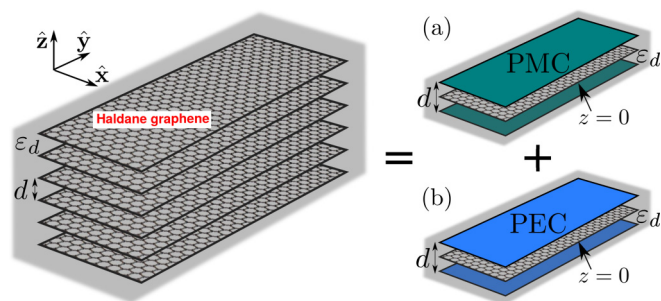
FIG. 4. The system under study: a periodic arrangement of Haldane graphene sheets with periodicity d is embedded in a dielectric with permittivity ε_d. The electromagnetic modes of this structure are the direct sum of the modes supported by a Haldane graphene sheet embedded in (a) a PMC-walls waveguide and (b) a PEC-walls waveguide, with walls located at $z = \pm d/2$.

an electron gas is always nontrivial even when B_0 is set identical to zero because the free-electron concentration is finite. Thus, the physical platform discussed in this article has quite unique properties, and generically behaves differently from a 2D magnetized plasma, particularly when the time-reversal symmetry is preserved.

IV. PHOTONIC TOPOLOGICAL PROPERTIES

Next, we characterize the photonic topological properties of the Haldane graphene. In particular, we study the low-frequency photonic phase transition induced by an electronic transition between the insulating and Hall phases, and highlight the relation between the nontrivial electronic and photonic topologies.

The rigorous definition of Chern numbers is only possible for an electromagnetically closed system, and thereby an isolated Haldane graphene sheet does not provide a suitable platform to observe a photonic topological phase transition. This problem can be circumvented by placing the Haldane graphene in some sort of waveguide environment that restricts the energy flow to directions parallel to the xoy plane [50]. However, the topological properties of such a quasi-2D waveguide may depend not only on the Haldane graphene but also on the waveguide top and bottom walls. To avoid such a problem, we consider instead a periodic arrangement of Haldane graphene sheets separated by a distance d and embedded in a dielectric with permittivity ε_d, as shown in Fig. 4. With this solution the topological properties of the system are determined only by the Haldane graphene.

As mentioned, we are interested in waves with energy flows restricted to directions parallel to the xoy plane. Due to symmetry reasons the electromagnetic modes (periodic in z) of the periodic system can be split into two subsets depending on the parity of the fields with respect to the plane $z = -d/2$: the modes of a waveguide with perfect magnetic conducting (PMC) walls (with H_z even and E_z odd) and the modes of a waveguide with perfect electric conducting (PEC) walls (with H_z odd and E_z even) as illustrated in Fig. 4. Note that the designations even and odd are used here with respect to a reference system with origin in the plane $z = -d/2$. It is highlighted that the PEC and PMC boundary conditions are

not imposed arbitrarily, but rather emerge naturally from the geometry of the periodic array.

Importantly, it can be shown that for a waveguide with PEC walls [system of Fig. 4(b)] all the modes that interact with the Haldane graphene are cut off at low frequencies. This means that to study the low frequency modes of the periodic arrangement of Haldane graphene sheets it is enough to consider the system of Fig. 4(a), being implicit that the excitation should respect the indicated parity symmetry of the fields. For this reason, in the rest of this paper we will restrict our attention to the system with PMC walls of Fig. 4(a).

A. Natural modes

Next, we derive the natural (guided) modes supported by the structure of Fig. 4(a). Because the system is invariant to translations along the x and y directions, the guided waves depend on the x and y coordinates as $e^{i\mathbf{q} \cdot \mathbf{r}}$ with $\mathbf{q} = q_x \hat{\mathbf{x}} + q_y \hat{\mathbf{y}}$ the (transverse) wave vector. Furthermore, in the dielectric regions the guided modes are superposition of plane waves. The modes may be split into modes with H_z even and modes with H_z odd (here the designations even and odd are with respect to the $z = 0$ plane). The modes with H_z odd do not interact with the Haldane graphene sheet, and hence are not interesting to us. They have a dispersion of the form $\omega_{n\mathbf{q}}^{\mathrm{odd}} = \frac{c}{\sqrt{\varepsilon_d}} \sqrt{q^2 + [(2n+1)\frac{\pi}{d}]^2}$, with $n = 0, 1, 2, \ldots$, and hence are cut off for low frequencies.

As to the modes with H_z even, a straightforward analysis shows that the electromagnetic field distribution that satisfies the PMC boundary conditions ($\hat{\mathbf{z}} \times \mathbf{H}_{z=-d/2} = \hat{\mathbf{z}} \times \mathbf{H}_{z=d/2} = 0$) and ensures the continuity of the tangential electric field at the graphene-dielectric interface is of the form

$$\mathbf{H}(\mathbf{r}) = e^{i\mathbf{q} \cdot \mathbf{r}} \left\{ \mathrm{sgn}(z) \sinh\left(\gamma_0\left[\frac{d}{2} - |z|\right]\right)(C_1 \mathbf{q} \times \hat{\mathbf{z}} + C_2 \mathbf{q}) \right.$$
$$\left. + i \frac{q^2}{\gamma_0} C_2 \cosh\left(\gamma_0\left[\frac{d}{2} - |z|\right]\right)\hat{\mathbf{z}} \right\}, \tag{10a}$$

$$\mathbf{E}(\mathbf{r}) = \frac{i e^{i\mathbf{q} \cdot \mathbf{r}}}{\omega \varepsilon_0 \varepsilon_d} \left\{ \cosh\left(\gamma_0\left[\frac{d}{2} - |z|\right]\right) \right.$$
$$\times \left[-\gamma_0 C_1 \mathbf{q} + C_2\left(\gamma_0 - \frac{q^2}{\gamma_0}\right)\mathbf{q} \times \hat{\mathbf{z}} \right]$$
$$\left. - i C_1 \mathrm{sgn}(z) q^2 \sinh\left(\gamma_0\left[\frac{d}{2} - |z|\right]\right)\hat{\mathbf{z}} \right\}, \tag{10b}$$

where $\gamma_0 = \sqrt{q^2 - \varepsilon_d \omega^2/c^2}$, $q = \sqrt{q_x^2 + q_y^2}$, and C_1, C_2 are (unknown) complex-valued coefficients. Using the boundary condition for the tangential component of the magnetic field at the graphene-dielectric interface $\hat{\mathbf{z}} \times (\mathbf{H}_{z=0^+} - \mathbf{H}_{z=0^-}) = \sigma^{\mathrm{gr}} \cdot \mathbf{1}_t \cdot \mathbf{E}$, one obtains the following homogeneous system of equations:

$$\begin{pmatrix} \frac{2i\omega\varepsilon_0\varepsilon_d}{\gamma_0} - \sigma_t \coth\left(\gamma_0 \frac{d}{2}\right) & -\sigma_H \coth\left(\gamma_0 \frac{d}{2}\right)\left(\frac{\gamma_0^2 - q^2}{\gamma_0^2}\right) \\ \sigma_H \coth\left(\gamma_0 \frac{d}{2}\right)\left(\frac{\gamma_0^2}{\gamma_0^2 - q^2}\right) & -\sigma_t \coth\left(\gamma_0 \frac{d}{2}\right) + \frac{-2i\gamma_0}{\omega\mu_0} \end{pmatrix} \begin{pmatrix} C_1 \\ C_2 \end{pmatrix}$$
$$= 0, \tag{11}$$

whose nontrivial solutions give the natural modes of oscillation of the system. The dispersion equation is obtained by setting
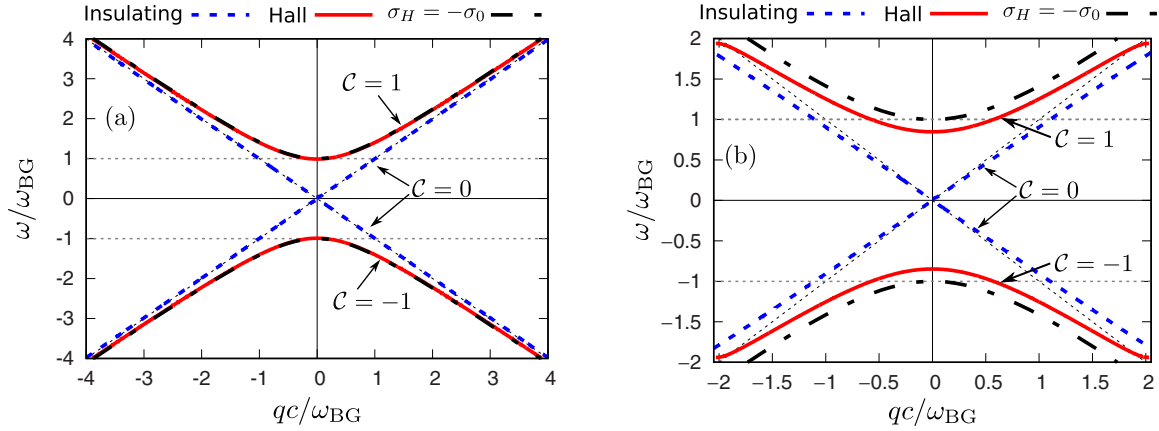
FIG. 5. Dispersion diagram of the lowest (positive and negative) frequency modes for $\varepsilon_d = 1$ and (a) $d = 2$ cm corresponding to $\omega_{BG} \approx 0.22$ GHz and (b) $d = 1$ mm corresponding to $\omega_{BG} \approx 4.38$ GHz. The curves associated with the insulating phase were obtained with the conductivity of Fig. 2(a) and the curves associated with the Hall phase with the conductivity of Fig. 2(b). The curves labeled by $\sigma_H = -\sigma_0$ correspond to the analytical solution (14) for the simplified conductivity model $\sigma_t = 0$ and $\sigma_H = -\sigma_0$. The photonic Chern number $\mathcal{C}$ for each dispersion branch is given in the insets.

the determinant of the matrix identical to zero

$$\left[2i \frac{\omega \varepsilon_0 \varepsilon_d}{\gamma_0} - \sigma_t \coth\left(\gamma_0 \frac{d}{2}\right) \right]\left[- \sigma_t \coth\left(\gamma_0 \frac{d}{2}\right) \right.$$
$$\left. + 2i \frac{\gamma_0}{-\omega \mu_0} \right] + \sigma_H^2 \coth^2\left(\gamma_0 \frac{d}{2}\right) = 0. \quad (12)$$

The solutions $\omega = \omega_{n\mathbf{q}}$ of the above equation determine the photonic band diagram. It is interesting to note that the limit $\gamma_0 d \to \infty$ yields the standard dispersion equation of magnetoplasmons [47,51,52] (with no PMC walls). Furthermore, a similar analysis shows that the dispersion of a waveguide with PEC walls is given by a similar expression with "tanh" in the place of "coth."

The electromagnetic modes $\mathbf{E}_{n\mathbf{q}}$, $\mathbf{H}_{n\mathbf{q}}$ associated with a given $\omega_{n\mathbf{q}}$, are obtained from Eqs. (10a) and (10b) with the coefficients C_1 and C_2 given by [see Eq. (11)]

$$C_1 = \sigma_H \coth\left(\gamma_{0,n\mathbf{q}} \frac{d}{2}\right)\left(\frac{\gamma_{0,n\mathbf{q}}^2 - q^2}{\gamma_{0,n\mathbf{q}}^2} \right), \quad (13a)$$

$$C_2 = 2i \frac{\omega_{n\mathbf{q}} \varepsilon_0 \varepsilon_d}{\gamma_{0,n\mathbf{q}}} - \sigma_t \coth\left(\gamma_{0,n\mathbf{q}} \frac{d}{2}\right), \quad (13b)$$

and $\gamma_{0,n\mathbf{q}} = \sqrt{q^2 - \varepsilon_d \omega_{n\mathbf{q}}^2/c^2}$.

It is useful to analyze the solutions of the dispersion equation (12) for a conductivity model with $\sigma_t = 0$ and a constant (frequency independent) σ_H. For $\sigma_H = \pm \sigma_0$ this model reduces to the static conductivity of Haldane graphene in the Hall phase. It yields the modal dispersion:

$$\omega_{n\mathbf{q}}^{even} \approx \frac{c}{\sqrt{\varepsilon_d}} \sqrt{q^2 + \left[\frac{2}{d} \arctan\left(\sqrt{\frac{\mu_0}{\varepsilon_0 \varepsilon_d}} \frac{\sigma_H}{2} \right) + \frac{2\pi n}{d} \right]^2}, \quad (14)$$

with $n = 0, 1, \ldots$. The modes with $n \geqslant 1$ are evidently cut off for low frequencies, and hence in the following we focus on the mode with $n = 0$. In the limit $\sigma_H = 0$ this mode follows the light line, and is clearly a transverse

electromagnetic (TEM) wave with magnetic field along z and electric field parallel to the plates. For a finite σ_H, the $n = 0$ mode interacts with the Haldane graphene sheet and this opens a band gap in the dispersion diagram, with a cut-off frequency $\omega_{BG} \equiv \frac{2c}{d\sqrt{\varepsilon_d}} \arctan\left(\sqrt{\frac{\mu_0}{\varepsilon_0 \varepsilon_d}} \frac{\sigma_H}{2} \right)$. The cut-off frequency is inversely proportional to the distance between the waveguide walls and approaches zero when $\sigma_H \to 0$. The attenuation factor in the direction normal to the graphene plane is $\gamma_{0,\mathbf{q}} = \frac{2i}{d} \arctan\left(\sqrt{\frac{\mu_0}{\varepsilon_0 \varepsilon_d}} \frac{\sigma_H}{2} \right)$, and hence it is pure imaginary for $\sigma_H \neq 0$ implying that the natural mode is not guided by the 2D material but rather by the waveguide walls.

In the case of a quantized Hall conductivity $\sigma_H = \sigma_0$, the cut-off frequency can be expressed in terms of the fine structure constant α: $\omega_{BG} = \frac{2c}{d\sqrt{\varepsilon_d}} \arctan\left(\frac{\alpha}{\sqrt{\varepsilon_d}} \right)$ and the associated wavelength (in host dielectric) at the gap edge is well approximated by $\lambda_{gap} \approx \frac{\pi \sqrt{\varepsilon_d} d}{\alpha} \approx 430.5 \sqrt{\varepsilon_d} d$. Thus, for this small value of σ_H the distance d is ultrasubwavelength at the cut-off frequency.

B. Band diagrams and photonic Chern numbers

Figure 5 shows the low-frequency photonic band diagram for the different electronic topological phases of Haldane graphene and two values of the distance d. In this calculation we used the conductivity responses of Fig. 2. Note that the photonic band diagram shows both positive and negative frequency solutions.

Consistent with Sec. IV A, the band diagrams reveal (for both values of d) that the dispersions induced by the distinct electronic phases are different: in the insulating phase the dispersions follow closely the light line, whereas in the Hall phase the diagram has a low-frequency band gap. The modes in the insulating phase lie outside the light cone and hence are guided by the graphene sheet. In contrast, in the Hall phase the dispersion lies inside the light cone and the wave is—as predicted by the static conductivity model—guided by the waveguide walls. Furthermore, as seen in Fig. 2 the static conductivity model with $\sigma_t = 0$ and $\sigma_H = -\sigma_0$ gives overall

a fairly good approximation of the modal dispersion. The approximation is better for larger values of d, when $\omega_{BG} \ll \omega_{max}$ with $\omega_{max} = E_g/\hbar$ the interband absorption threshold.

From the eigenmodes expressions (10a) and (10b) it is possible to compute the Chern number for each photonic band. The calculation details are given in Appendix B. The approach is based on an extension to layered structures of the theory of [10,41].

The values of the photonic Chern number for each branch are depicted as insets in Fig. 5. The photonic Chern number of the bands associated with the electronic insulating phase vanishes because of the time-reversal symmetry of the system. We note in passing that the Chern number of a set of touching bands has always an unambiguous value, even though generically the Chern number of the individual bands may be ill-defined when there are band-crossing points. In contrast, the Chern numbers of the Hall phase are nontrivial with values $\mathcal{C} = \pm 1$. Thus, the electronic topological transition from the insulating to the Hall phase (see Fig. 3) induces the band-gap opening at $\omega = 0$ accompanied by the exchange of photonic Chern numbers between the positive and negative frequency bands, and thereby a photonic topological phase transition. As expected [53], the total Chern number for each phase is conserved throughout this transition. Remarkably, the topological photonic properties of the material are directly linked to its electronic counterparts such that the electronic Chern number of the valence band is equal to the photonic Chern number of the positive frequency branch: $\mathcal{C} = \nu = -\sigma_H^s/\sigma_0$, as shown in Fig. 3(b). This result proves that a magnetic field bias with a vanishing flux enables a nontrivial photonic topology, similar to the Haldane result for the electronic case.

C. Unidirectional edge states

According to the bulk-edge correspondence [10], one may expect that an interface of the Hall phase of Haldane graphene and a trivial photonic insulator may support topologically protected edge states that span the entire common band gap. The existence of such unidirectional topologically protected edge states is demonstrated next with full wave simulations. The trivial photonic insulator is implemented with the same

waveguide but with a PEC plate in the place of the Haldane graphene. It may be checked that the modes supported by such a structure are cut off in the long wavelength limit.

We used CST Microwave Studio [54] to demonstrate the emergence of the topological edge states. The optical response of a 2D material sheet with 2D conductivity σ^{gr} can be emulated with an equivalent 3D material with thickness h_0 and an equivalent permittivity $\boldsymbol{\varepsilon}/\varepsilon_0 = \mathbf{1} + i\frac{\sigma^{gr}}{h_0\omega\varepsilon_0}$. The thickness h_0 must be much smaller than the wavelengths of interest and in addition $h_0 \ll d$. It was taken equal to $h_0 = d/10$ in the numerical study.

The Haldane graphene conductivity in the Hall phase is as shown in Fig. 2(b). The waveguide height is $d = 400\ \mu$m. The structure is excited with a small dipole antenna (polarized along the x direction) located in the close proximity of the interface of the two waveguide regions, with the oscillation frequency in the band gap ($\omega < \omega_{BG}$).

A time snapshot of the z component of the magnetic field is represented in Fig. 6(a) for $\omega \approx 0.62\omega_{BG}$. As seen, a unidirectional edge state propagating along the $+y$ direction is excited in the bottom region at the interface between the PEC material and Haldane graphene. A time animation of the magnetic field is available in the Supplemental Material [55] and further highlights that this edge state propagates along the interface, regardless of the sharp corners, before reaching an absorber on the right side region. By fitting the wavelength of the guided modes we numerically determined the dispersion of the edge states depicted in Fig. 6(b). Due to numerical limitations the dispersion of the edge mode is only represented in the band-gap frequency range. As seen, the edge modes span the entire band gap. Curiously, they follow closely the bulk dispersion of the insulating photonic phase of the Haldane graphene. The low frequency part of the curve was obtained by interpolation because the guided wavelength approaches infinity.

In the waveguide environment, the edge state is topologically protected against the scattering by an arbitrary three-dimensional defect, and in particular it is protected against sideways scattering [56]. The same property holds (for the relevant wave polarization, i.e., for quasitransverse magnetic waves) in a periodic array of Haldane graphene sheets, but in this case only for two-dimensional defects uniform along the
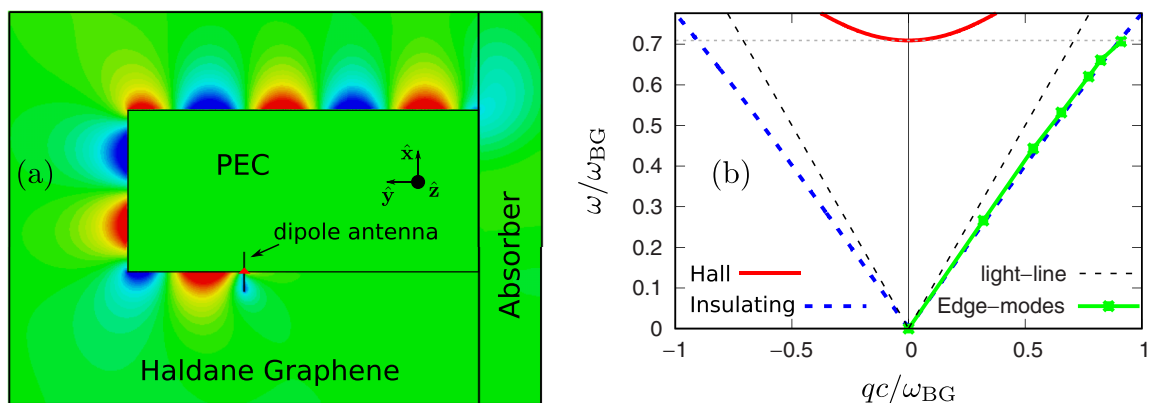

FIG. 6. (a) Time snapshot of the magnetic field H_z radiated by a short dipole antenna with $\omega = 0.62\omega_{BG}$ showing the excitation of the topological edge state. (b) Dispersion of the unidirectional edge modes supported by the system (discrete points joined by a solid line obtained by interpolation). The band structure of the bulk material in the Hall and insulating phases is also represented in the figure. In the plots the dielectric host is air ($\varepsilon_d = 1$) and the distance between the waveguide plates is $d = 400\ \mu$m.

z direction. Indeed, for a periodic material there are additional radiation channels, for example, the modes that propagate off-plane or the TEM wave with electric field normal to the graphene plane. Note that the constraint on the defects geometry and wave polarization also applies to conventional designs based on gyrotropic media [56].

In the numerical simulations the response of the Haldane graphene was assumed lossless (consistent with the theoretical model); we checked that the presence of moderate loss does not affect significantly the edge state propagation in the simulation (not shown).

V. CONCLUSIONS

The work developed in this article is divided into two parts. In the first part we verified using a first-principles mean field theory the validity of the Haldane model for a honeycomb lattice with broken TRS and IS. We proposed a magnetic field distribution that mimics the main features of Haldane's theory, and found the dependence of the tight-binding parameters on the magnetic field in artificial graphene. The electronic phase diagram showing the range of parameters for which the magnetized artificial graphene is topologically nontrivial and the quantized Hall conductivity is nonzero was determined.

In the second part, we investigated the optical response of the 2D topological material. The dynamic electric conductivity of Haldane graphene was found with the Kubo formula for a filled valence band. Using this result, we determined the guided modes and the (low-frequency) photonic band diagram of a periodic stack of Haldane graphene sheets. As a fingerprint of the quantized conductivity, the cut-off frequency of the low-frequency band gap is written in terms of the fine structure constant.

Furthermore, our analysis reveals that the electronic phase transition between the insulating and Hall phases induces a photonic phase transition through the opening of a band gap at $\omega = 0$ and an exchange of Chern numbers between the positive and negative frequency bands. Interestingly, the electronic and photonic topological properties of this system are intimately related, and we find that the electronic and photonic Chern numbers are identical. In particular, our results imply that a biasing magnetic field with zero net flux can induce a nontrivial topological photonic response. Finally, in agreement with the bulk-edge correspondence, it was shown that the nontrivial photonic phase of Haldane graphene supports topologically protected unidirectional edge states at the interface with an ordinary photonic insulator.

ACKNOWLEDGMENTS

APPENDIX A: THE ELECTRONIC CHERN NUMBER

In the framework of the exact Haldane Hamiltonian, the electronic Chern number of the nth band is given by

$$\nu_n = \frac{1}{2\pi} \int\int_{BZ} d^2\mathbf{k} \, \hat{\mathbf{z}} \cdot \nabla \times \mathcal{A}_{n\mathbf{k}}, \tag{A1}$$

where $\mathcal{A}_{n\mathbf{k}}$ is the Berry potential and the integration is over the entire Brillouin zone. The Berry potential is written in terms of the energy eigenfunctions. A suitable globally defined gauge of eigenfunctions for the valence band $|-\rangle$ is

$$\psi_{\mathbf{k}} = \begin{pmatrix} -h_{12}(\mathbf{k}) \\ h_{11}(\mathbf{k}) - E_-(\mathbf{k}) \end{pmatrix}. \tag{A2}$$

In the above, h_{ij} with $i,j = 1,2$ represent the elements of the exact Haldane Hamiltonian and E_- is the exact energy dispersion of the valence band (see Eq. (1) of Ref. [36]). The Berry potential of the valence band is given by

$$\mathcal{A}_{n\mathbf{k}} = \frac{\mathrm{Re}\{i\psi_{\mathbf{k}}^* \cdot \partial_{\mathbf{k}} \psi_{\mathbf{k}}\}}{\psi_{\mathbf{k}}^* \cdot \psi_{\mathbf{k}}}. \tag{A3}$$

It is evidently a smooth function of the wave vector, except possibly at the points wherein the considered gauge vanishes, i.e., at the points of the Brillouin zone for which $h_{12}(\mathbf{k}) = 0$ and $h_{11}(\mathbf{k}) = E_-(\mathbf{k})$. A straightforward analysis using the analytical formula of h_{12} [36] reveals that the only possible singularities are the high-symmetry points K and K'. Hence, using Stokes theorem it is possible to reduce the calculation of the valence band Chern number to two contour integrals surrounding the points K and K':

$$\nu = -\frac{1}{2\pi} \sum_{i=K,K'} \oint_{C_i} \mathcal{A}_{\mathbf{k}} \cdot \mathbf{dl}. \tag{A4}$$

Here C_i stands for a circumference (with anticlockwise orientation) of arbitrarily small radius centered at the point $i = K, K'$. Explicit calculations show that

$$\frac{1}{2\pi} \oint_{C_i} \mathcal{A}_{\mathbf{k}} \cdot \mathbf{dl} = s_i \frac{1}{2}[1 - \mathrm{sgn}(\alpha_i)], \tag{A5}$$

with $s_K = 1$ and $s_{K'} = -1$. Substitution of this result into Eq. (A4) yields the electronic Chern number (4).

APPENDIX B: THE PHOTONIC CHERN NUMBER

In this Appendix we present the derivation of the Berry potential and photonic Chern number for the system of Fig. 4. The derivation is an extension of the theory developed in [41,50,57] to the case of z-stratified inhomogeneous closed systems. For the sake of brevity, we reuse here the notations and concepts introduced in [41]. For more information the reader is referred to [41,50].

The electromagnetic modes of the system satisfy the homogeneous Maxwell's equations

$$\hat{N} \cdot \mathbf{f} = \omega \mathbf{M} \cdot \mathbf{f}, \tag{B1}$$

where $\mathbf{f} = (\mathbf{E} \quad \mathbf{H})^T$ is a six-vector whose components are the electric and the magnetic fields. In the above, $\hat{N}$ is a differential operator

$$\hat{N} = \begin{pmatrix} 0 & i\nabla \times \mathbf{1}_{3\times 3} \\ -i\nabla \times \mathbf{1}_{3\times 3} & 0 \end{pmatrix}, \tag{B2}$$

and $\mathbf{M}$ is the material matrix. For the system of Fig. 4 with a conductivity sheet centered at $z = 0$, the material matrix is of

the form

$$\mathbf{M}(\mathbf{r}) = \mathbf{M}_d + \delta(z) \begin{pmatrix} \dfrac{\boldsymbol{\sigma}}{-i\omega} & 0 \\ 0 & 0 \end{pmatrix}, \tag{B3}$$

where $\boldsymbol{\sigma}$ is the 2D conductivity and $\mathbf{M}_d = \begin{pmatrix} \varepsilon_0 \varepsilon_d \mathbf{1}_{3\times 3} & 0 \\ 0 & \mu_0 \mathbf{1}_{3\times 3} \end{pmatrix}$ is the material matrix of the surrounding dielectric. The topological classification of the system is only possible if the conductivity is a meromorphic function of frequency [41,50,57], and thereby here we use the low-frequency conductivity model (9).

The electromagnetic fields are Bloch waves $\mathbf{f}(\mathbf{r}) = \mathbf{f}_{n\mathbf{q}}(z)e^{i\mathbf{q}\cdot\mathbf{r}}$, where the field envelope $\mathbf{f}_{n\mathbf{q}}$ depends only on the z coordinate and $\mathbf{q} = q_x\hat{\mathbf{x}} + q_y\hat{\mathbf{y}}$. The Berry potential $\mathcal{A}_{n\mathbf{q}}$ is defined from the Hermitian formulation of the Maxwell equations, and can be written as

$$\mathcal{A}_{n\mathbf{q}} = \frac{i\langle \mathbf{Q}_{n\mathbf{q}} | \partial_{\mathbf{q}} \mathbf{Q}_{n\mathbf{q}} \rangle}{\langle \mathbf{Q}_{n\mathbf{q}} | \mathbf{Q}_{n\mathbf{q}} \rangle}, \tag{B4}$$

where the $\mathbf{Q}_{n\mathbf{q}}$'s are generalized state vectors (see [41]), $\langle \ | \ \rangle$ denotes a weighted inner product and $\partial_{\mathbf{q}} \equiv \frac{\partial}{\partial \mathbf{q}}$. In the case of a z-stratified inhomogeneous system, the weighted inner product may be defined such that

$$\langle \mathbf{Q}_{n\mathbf{q}} | \mathbf{Q}_{n\mathbf{q}} \rangle = \frac{1}{2} \int_{-d/2}^{d/2} \mathbf{f}_{n\mathbf{q}}^* \cdot \frac{\partial}{\partial \omega} [\omega \mathbf{M}] \cdot \mathbf{f}_{n\mathbf{q}} dz. \tag{B5}$$

Furthermore, it can be shown that the numerator of Eq. (B4) satisfies

$$i\langle \mathbf{Q}_{n\mathbf{q}} | \partial_{\mathbf{q}} \mathbf{Q}_{n\mathbf{q}} \rangle = \mathrm{Re}\left\{ \frac{1}{2} \int_{-d/2}^{d/2} \mathbf{f}_{n\mathbf{q}}^* \cdot \frac{\partial}{\partial \omega} [\omega \mathbf{M}] \cdot i \frac{\partial}{\partial \mathbf{q}} \mathbf{f}_{n\mathbf{q}} dz \right\}. \tag{B6}$$

The previous results generalize Eqs. (10) and (14) of [41] to the case of z-stratified closed systems. In particular, for the geometry of Fig. 4, the Berry potential (B4) is given by

$$\mathcal{A}_{n\mathbf{q}} = \frac{\mathrm{Re}\left(\frac{1}{2} \int_{-d/2}^{d/2} \mathbf{f}_{n\mathbf{q}}^* \cdot \partial_{\omega}(\omega \mathbf{M}_d)_{\omega_{n\mathbf{q}}} \cdot i \partial_{\mathbf{q}} \mathbf{f}_{n\mathbf{q}} dz + \frac{1}{2} \mathbf{E}_{\mathrm{tan},\mathbf{q}}^*(z=0) \cdot \partial_{\omega}(i\boldsymbol{\sigma})_{\omega_{n\mathbf{q}}} \cdot i \partial_{\mathbf{q}} \mathbf{E}_{\mathrm{tan},\mathbf{q}}(z=0) \right)}{\frac{1}{2} \int_{-d/2}^{d/2} \mathbf{f}_{n\mathbf{q}}^* \cdot \partial_{\omega}(\omega \mathbf{M}_d)_{\omega_{n\mathbf{q}}} \cdot \mathbf{f}_{n\mathbf{q}} dz + \frac{1}{2} \mathbf{E}_{\mathrm{tan},\mathbf{q}}^*(z=0) \cdot \partial_{\omega}(i\boldsymbol{\sigma})_{\omega_{n\mathbf{q}}} \cdot \mathbf{E}_{\mathrm{tan},\mathbf{q}}(z=0)}, \tag{B7}$$

where $\mathbf{E}_{\mathrm{tan},\mathbf{q}} = \mathbf{1}_t \cdot \mathbf{E}_{n\mathbf{q}}$ is the part of the electric field tangential to the conductivity sheet and $\partial_{\omega} \equiv \frac{\partial}{\partial \omega}$.

As explained in [41], for systems invariant under rotations about the z axis the Chern number of a given band is simply

$$\mathcal{C}_n = \lim_{q \to \infty} (q \mathcal{A}_{n\mathbf{q},\varphi}) - \lim_{q \to 0^+} (q \mathcal{A}_{n\mathbf{q},\varphi}), \tag{B8}$$

where $\mathcal{A}_{n\mathbf{q},\varphi} = \mathcal{A}_{n\mathbf{q}} \cdot \hat{\boldsymbol{\varphi}}$ and $\hat{\boldsymbol{\varphi}}$ is the azimuthal unit vector in a system of polar coordinates. Even though the 2D wave vector space is unbounded, for a nondispersive dielectric host and for the model (9) the Chern number is necessarily an integer because for any band $\omega_{n\mathbf{q}} \to \infty$ in the $\mathbf{q} \to \infty$ limit, and the response becomes reciprocal when $\omega \to \infty$ [41]. In general, the topological classification of a continuum is only possible with the proper regularization of the material response with a high-frequency spatial cut off [10,41] (see also Ref. [58]). As further discussed in Ref. [41], when the material response has a spatial cut off—such that it is asymptotically the same as that of the electromagnetic vacuum—the equivalent Hamiltonian is sufficiently "well behaved" in the $\mathbf{q} \to \infty$ limit (albeit not continuous) and the gap Chern numbers are

integers. It is worth to highlight that the well-behaved condition is stronger than imposing that the relevant Hamiltonian becomes time-reversal invariant in the $\mathbf{q} \to \infty$ limit. In particular, an extension of the theory of Ref. [41] to generic physical systems (e.g., to some condensed matter platforms) may require a suitable cut-off procedure that ensures that the well-behaved condition is observed. A cut-off procedure that only guarantees that the Hamiltonian is asymptotically time-reversal invariant is generically inadequate.

It should be noted that the topological classification of the photonic phase relies on the conductivity of the Haldane graphene, which models the electron gas as a continuum, i.e., it disregards its intrinsic periodicity. Thus, it relies on an effective medium theory which, generally speaking, may be inadequate the model the physics near the edges of the Brillouin zone. Despite this limitation, our topological classification of the photonic phase is still full of physical meaning: it enables one to predict the "low" wave number edge states that can be described by the "continuum" conductivity model. This is evidently the case of the edge states found in Fig. 6(b), which have dispersion near the light line.

[1] M. Z. Hasan and C. L. Kane, *Colloquium*: Topological insulators, Rev. Mod. Phys. **82**, 3045 (2010).

[2] S.-Q. Shen, *Topological Insulators*, Springer Series in Solid-State Sciences, Vol. 174 (Springer, Berlin, 2012).

[3] L. Lu, J. D. Joannopoulos, and M. Soljačić, Topological photonics, Nat. Photon. **8**, 821 (2014).

[4] L. Lu, J. D. Joannopoulos, and M. Soljačić, Topological states in photonic systems, Nat. Phys. **12**, 626 (2016).

[5] F. D. M. Haldane, Nobel lecture: Topological quantum matter, Rev. Mod. Phys. **89**, 040502 (2017).

[6] B. I. Halperin, Quantized Hall conductance, current-carrying edge states, and the existence of extended states in a two-dimensional disordered potential, Phys. Rev. B **25**, 2185 (1982).

[7] Y. Hatsugai, Chern Number and Edge States in the Integer Quantum Hall Effect, Phys. Rev. Lett. **71**, 3697 (1993).

[8] C. L. Kane and E. J. Mele, Z_2 Topological Order and the Quantum Spin Hall Effect, Phys. Rev. Lett. **95**, 146802 (2005).

[9] S. Raghu and F. D. M. Haldane, Analogs of quantum-Hall-effect edge states in photonic crystals, Phys. Rev. A **78**, 033834 (2008).

[10] M. G. Silveirinha, Bulk-edge correspondence for topological photonic continua, Phys. Rev. B **94**, 205105 (2016).

[11] R. E. Camley, Nonreciprocal surface waves, Surf. Sci. Rep. **7**, 103 (1987).

[12] L. E. Zhukov and M. E. Raikh, Chiral electromagnetic waves at the boundary of optical isomers: Quantum Cotton-Mouton effect, Phys. Rev. B **61**, 12842 (2000).

[13] F. D. M. Haldane and S. Raghu, Possible Realization of Directional Optical Waveguides in Photonic Crystals with Broken Time-Reversal Symmetry, Phys. Rev. Lett. **100**, 013904 (2008).

[14] Z. Yu, G. Veronis, Z. Wang, and S. Fan, One-Way Electromagnetic Waveguide Formed at the Interface between a Plasmonic Metal under a Static Magnetic Field and a Photonic Crystal, Phys. Rev. Lett. **100**, 023902 (2008).

[15] Z. Wang, Y. Chong, J. D. Joannopoulos, and M. Soljačić, Observation of unidirectional backscattering-immune topological electromagnetic states, Nature (London) **461**, 772 (2009).

[16] T. Ochiai and M. Onoda, Photonic analog of graphene model and its extension: Dirac cone, symmetry, and edge states, Phys. Rev. B **80**, 155103 (2009).

[17] X. Ao, Z. Lin, and C. T. Chan, One-way edge mode in a magneto-optical honeycomb photonic crystal, Phys. Rev. B **80**, 033105 (2009).

[18] Y. Poo, R.-X. Wu, Z. Lin, Y. Yang, and C. T. Chan, Experimental Realization of Self-Guiding Unidirectional Electromagnetic Edge States, Phys. Rev. Lett. **106**, 093903 (2011).

[19] K. Fang, Z. Yu, and S. Fan, Realizing effective magnetic field for photons by controlling the phase of dynamic modulation, Nat. Photon. **6**, 782 (2012).

[20] A. R. Davoyan and N. Engheta, Theory of Wave Propagation in Magnetized Near-Zero-Epsilon Metamaterials: Evidence for One-Way Photonic States and Magnetically Switched Transparency and Opacity, Phys. Rev. Lett. **111**, 257401 (2013).

[21] A. Davoyan and N. Engheta, Electrically controlled one-way photon flow in plasmonic nanostructures, Nat. Commun. **5**, 5250 (2014).

[22] S. A. Skirlo, L. Lu, Y. Igarashi, Q. Yan, J. Joannopoulos, and M. Soljačić, Experimental Observation of Large Chern Numbers in Photonic Crystals, Phys. Rev. Lett. **115**, 253901 (2015).

[23] F. Abbasi, A. R. Davoyan, and N. Engheta, One-way surface states due to nonreciprocal light-line crossing, New J. Phys. **17**, 063014 (2015).

[24] M. Minkov and V. Savona, Haldane quantum Hall effect for light in a dynamically modulated array of resonators, Optica **3**, 200 (2016).

[25] D. Jin, L. Lu, Z. Wang, C. Fang, J. D. Joannopoulos, M. Soljačić, L. Fu, and N. X. Fang, Topological magnetoplasmon, Nat. Commun. **7**, 13486 (2016).

[26] C. He, X.-C. Sun, X.-P. Liu, M.-H. Lu, Y. Chen, L. Feng, and Y.-F. Chen, Photonic topological insulator with broken time-reversal symmetry, Proc. Natl. Acad. Sci. USA **113**, 4924 (2016).

[27] D. Jin, T. Christensen, M. Soljačić, N. X. Fang, L. Lu, and X. Zhang, Infrared Topological Plasmons in Graphene, Phys. Rev. Lett. **118**, 245301 (2017).

[28] M. Hafezi, E. A. Demler, M. D. Lukin, and J. M. Taylor, Robust optical delay lines with topological protection, Nat. Phys. **7**, 907 (2011).

[29] M. C. Rechtsman, J. M. Zeuner, Y. Plotnik, Y. Lumer, D. Podolsky, F. Dreisow, S. Nolte, M. Segev, and A. Szameit, Photonic Floquet topological insulators, Nature (London) **496**, 196 (2013).

[30] A. B. Khanikaev, S. H. Mousavi, W.-K. Tse, M. Kargarian, A. H. MacDonald, and G. Shvets, Photonic topological insulators, Nat. Mater. **12**, 233 (2013).

[31] W. Gao, M. Lawrence, B. Yang, F. Liu, F. Fang, B. Béri, J. Li, and S. Zhang, Topological Photonic Phase in Chiral Hyperbolic Metamaterials, Phys. Rev. Lett. **114**, 037402 (2015).

[32] F. Liu and J. Li, Gauge Field Optics with Anisotropic Media, Phys. Rev. Lett. **114**, 103902 (2015).

[33] W.-J. Chen, Z.-Q. Zhang, J.-W. Dong, and C. T. Chan, Symmetry-protected transport in a pseudospin-polarized waveguide, Nat. Commun. **6**, 8183 (2015).

[34] A. Slobozhanyuk, S. H. Mousavi, X. Ni, D. Smirnova, Y. S. Kivshar, and A. B. Khanikaev, Three-dimensional all-dielectric photonic topological insulator, Nat. Photon. **11**, 130 (2017).

[35] M. G. Silveirinha, $\mathcal{P} \cdot \mathcal{T} \cdot \mathcal{D}$ symmetry-protected scattering anomaly in optics, Phys. Rev. B **95**, 035153 (2017).

[36] F. D. M. Haldane, Model for a Quantum Hall Effect without Landau Levels: Condensed-Matter Realization of the "Parity Anomaly", Phys. Rev. Lett. **61**, 2015 (1988).

[37] W. J. M. Kort-Kamp, B. Amorim, G. Bastos, F. A. Pinheiro, F. S. S. Rosa, N. M. R. Peres, and C. Farina, Active magneto-optical control of spontaneous emission in graphene, Phys. Rev. B **92**, 205415 (2015).

[38] L. Cai, M. Liu, S. Chen, Y. Liu, W. Shu, H. Luo, and S. Wen, Quantized photonic spin Hall effect in graphene, Phys. Rev. A **95**, 013809 (2017).

[39] M. Gibertini, A. Singha, V. Pellegrini, M. Polini, G. Vignale, A. Pinczuk, L. N. Pfeiffer, and K. W. West, Engineering artificial graphene in a two-dimensional electron gas, Phys. Rev. B **79**, 241406 (2009).

[40] S. Lannebère and M. G. Silveirinha, Effective Hamiltonian for electron waves in artificial graphene: A first-principles derivation, Phys. Rev. B **91**, 045416 (2015).

[41] M. G. Silveirinha, Chern invariants for continuous media, Phys. Rev. B **92**, 125153 (2015).

[42] M. G. Silveirinha and N. Engheta, Effective medium approach to electron waves: Graphene superlattices, Phys. Rev. B **85**, 195413 (2012).

[43] N. Nagaosa, J. Sinova, S. Onoda, A. H. MacDonald, and N. P. Ong, Anomalous hall effect, Rev. Mod. Phys. **82**, 1539 (2010).

[44] D. J. Thouless, M. Kohmoto, M. P. Nightingale, and M. den Nijs, Quantized Hall Conductance in a Two-Dimensional Periodic Potential, Phys. Rev. Lett. **49**, 405 (1982).

[45] R. Kubo, The fluctuation-dissipation theorem, Rep. Prog. Phys. **29**, 255 (1966).

[46] S. A. Mikhailov and K. Ziegler, New Electromagnetic Mode in Graphene, Phys. Rev. Lett. **99**, 016803 (2007).

[47] P. A. D. Gonçalves and N. M. R. Peres, *An Introduction to Graphene Plasmonics* (World Scientific, New Jersey, 2016).

[48] P. B. Allen, Electron Transport, in *Conceptual Properties of Materials, A Standard Model for Ground- and Excited-State Properties*, edited by S. G. Louie and M. L. Cohen (Elsevier, Amsterdam, 2006).

[49] J. A. Bittencourt, *Fundamentals of Plasma Physics*, 3rd ed. (Springer, New York, 2010).

[50] M. G. Silveirinha, Topological classification of Chern-type insulators by means of the photonic Green function, Phys. Rev. B **97**, 115146 (2018).

[51] K. W. Chiu and J. J. Quinn, Plasma oscillations of a two-dimensional electron gas in a strong magnetic field, Phys. Rev. B **9**, 4724 (1974).

[52] A. Ferreira, N. M. R. Peres, and A. H. Castro Neto, Confined magneto-optical waves in graphene, Phys. Rev. B **85**, 205426 (2012).

[53] J. E. Avron, R. Seiler, and B. Simon, Homotopy and Quantization in Condensed Matter Physics, Phys. Rev. Lett. **51**, 51 (1983).

[54] CST, GmbH 2017 CST Microwave Studio, http://www.cst.com (2017).

[55] See Supplemental Material at http://link.aps.org/supplemental/10.1103/PhysRevB.97.165128 for the time animation of Fig. 6(a), showing the propagation of the unidirectional edge state along the interface.

[56] S. A. H. Gangaraj, A. Nemilentsau, and G. W. Hanson, The effects of three-dimensional defects on one-way surface plasmon propagation for photonic topological insulators comprised of continuum media, Sci. Rep. **6**, 30055 (2016).

[57] M. G. Silveirinha, Modal expansions in dispersive material systems with application to quantum optics and topological photonics, in Advances in Mathematical Methods for Electromagnetics, edited by P. Smith and K. Kobayashi (IET, to appear), available online in arXiv:1712.04272.

[58] S. Ryu, A. P. Schnyder, A. Furusaki, and A. W. W. Ludwig, Topological insulators and superconductors: Tenfold way and dimensional hierarchy, New J. Phys. **12**, 065010 (2010).